Plasmon polaritons in cubic lattices of spherical metallic nanoparticles

Simon Lamowski,[1,2] Charlie-Ray Mann,[3] Felicitas Hellbach,[1] Eros Mariani,[3] Guillaume Weick,[4,*] and Fabian Pauly[1,2,†]

[1]*Department of Physics and Center for Applied Photonics, University of Konstanz, D-78457 Konstanz, Germany*
[2]*Okinawa Institute of Science and Technology Graduate University, Onna-son, Okinawa 904-0395, Japan*
[3]*School of Physics and Astronomy, University of Exeter, Stocker Rd., Exeter EX4 4QL, United Kingdom*
[4]*Université de Strasbourg, CNRS, Institut de Physique et Chimie des Matériaux de Strasbourg, UMR 7504, F-67000 Strasbourg, France*

We theoretically investigate plasmon polaritons in cubic lattices of spherical metallic nanoparticles. The nanoparticles, each supporting triply-degenerate localized surface plasmons, couple through the Coulomb dipole-dipole interaction, giving rise to collective plasmons that extend over the whole metamaterial. The latter hybridize with photons forming plasmon polaritons, which are the hybrid light-matter eigenmodes of the system. We derive general analytical expressions to evaluate both plasmon and plasmon-polariton dispersions and the corresponding eigenstates. These are obtained within a Hamiltonian formalism, which takes into account retardation effects in the dipolar interaction between the nanoparticles and considers the dielectric properties of the nanoparticles as well as their surrounding. Within this model we predict polaritonic splittings in the near-infrared to the visible range of the electromagnetic spectrum that depend on polarization, lattice symmetry, and wave-vector direction. Finally, we show that the predictions of our model are in excellent quantitative agreement with conventional finite-difference frequency-domain simulations, but with the advantages of analytical insight and significantly reduced computational cost.

I. INTRODUCTION

Plasmonic metamaterials can be exploited to manipulate light at subwavelength scales and may be used to tailor optical properties [1–3]. They consist of meta-atoms with possibly complicated subwavelength structures that are arranged in a controlled fashion [4]. Potential applications of such metamaterials range from optical cloaking over planar hyperlenses to optical data processing [5,6].

The study of the optical properties of one-dimensional (1D), two-dimensional (2D), and three-dimensional (3D) arrays of metallic particles is a very active field of research [7]. In the past, most theoretical and experimental research has been focused on 1D and 2D systems, since they are much easier to fabricate with well-established techniques [3,4]. However, the development of reliable techniques to control 3D assemblies of plasmonic nanoparticles is presently making substantial advances, and such 3D assemblies can now be achieved by using surface ligands or DNA templates [7–11]. It is thus of current interest to also understand systematically the structure-property relationships in 3D crystalline arrangements of meta-atoms, where, beside the shape and the size of the nanoparticles themselves, the spacing and the crystal symmetry can be controlled independently.

The optical properties of a plasmonic metamaterial are governed in the first instance by those of the individual metallic nanoparticles [4]. Of primary importance to understand such optical properties are the localized surface plasmons (LSPs),

which correspond to collective oscillations of the valence electrons against the ionic background. The resonance frequency and polarization of the LSP modes are determined by the size, shape, and material of the nanoparticles.

Classical electrodynamics can be used to understand many of the optical properties of 1D, 2D, and 3D plasmonic metamaterials [2,7]. Depending on the distance between the meta-atoms, two qualitatively different regimes emerge [4]: In the first regime, the distance between the meta-atoms is on the order of or larger than the wavelength associated with the LSP resonance of individual nanoparticles, so that diffractive far-field interactions between the meta-atoms of the array can interfere, leading to collective modes termed surface lattice resonances. In the second, opposite regime, the meta-atom separation is much smaller than the LSP resonance wavelength so that near-field interactions are predominant, yielding collective plasmons that are extended over the whole metamaterial. In the present paper we concentrate on the latter regime.

Early studies on the plasmonic properties of near-field-coupled metallic nanoparticles focused on 1D chains using a nonretarded model of point dipoles [12–15], followed by fully-retarded classical approaches applied to 1D [16–25] and 2D systems [26–30]. Three-dimensional metastructures were also investigated using more approximate approaches such as the Maxwell-Garnett effective medium theory [7] or Bruggeman effective medium theory [31]. In addition to the classical, typically fully numerical treatments, an analytically tractable approach based on a Hamiltonian formalism was recently applied to 1D [32–35], 2D [36–38], and 3D systems [39].

In this paper we study the less explored 3D plasmonic arrays in the regime of near-field coupling between spherical metallic

*guillaume.weick@ipcms.unistra.fr
†fabian.pauly@oist.jp

nanoparticles. Spherical particles are chosen in order to focus on the effects of crystal structure on the optical properties only. The nature of the modes supported by a plasmonic metamaterial depends crucially on the dimensionality of the lattice. For 1D and 2D lattices, the collective plasmons couple to a continuum of photonic modes with different wave-vector components along directions where translational symmetry is absent. However, as it has been pointed out by Hopfield in the context of exciton polaritons [40], in stark contrast to lower dimensional systems, collective plasmons in 3D lattices only couple to photons which conserve crystal momentum due to the discrete translational symmetry of the system. As a result, the true eigenmodes of the metamaterial are coherent super-positions of plasmons and photons, which we call plasmon polaritons. We study them by means of an analytically tractable Hamiltonian-based approach, which importantly incorporates retardation effects.

In what follows we consider 3D lattices of spherical metal-lic nanoparticles, including simple cubic (sc), face-centered cubic (fcc), and body-centered cubic (bcc) structures. In the quasistatic limit [41], each nanoparticle supports a discrete set of multipolar LSP modes. However, as we consider small nanoparticles (of some 10 nm in radius), we neglect higher-order multipolar modes and focus on the fundamental dipolar LSPs, whose corresponding frequency lies in the visible to ultraviolet range of the spectrum. In this regime, quantum-size effects in the optical response of the nanoparticles can be significant [6]. Due to the spherical symmetry of the nanoparticles, each dipolar LSP is triply-degenerate with three polarization degrees of freedom.

We work in the Coulomb gauge [42,43], where the scalar and vector potentials describe the longitudinal and transverse components of the electromagnetic field, respectively. The scalar potential, which depends only on the matter degrees of freedom, takes the form of the instantaneous Coulomb interaction between the LSPs. This results in collective plas-monic modes, which extend across the whole metamaterial. The effects of retardation are then included in the light-matter coupling through the interaction of the LSPs with the transverse vector potential. In this way, transverse photons hybridize with the collective plasmons to form plasmon polaritons. We also take into account screening effects from the core electrons as well as the dielectric medium surrounding the nanoparticles.

Here, we decisively extend inspiring work of some of the authors [39]. Although it is stated in Ref. [39] that spherical metallic nanoparticles are used, these nanoparticles were assumed to exhibit only one polarization degree of freedom that was fixed in a given direction. This gives rise to a single plasmon band, whose polarization does not depend on the wave vector. In fact this model does not correctly describe lattices of spherical nanoparticles, but could be used to study lattices of resonators that have a nondegenerate fundamental eigenmode, such as plasmonic nanorods. Our treatment fixes this issue by considering plasmon polaritons which arise from the hybridization of photons with three plasmonic bands with wave-vector-dependent polarizations. Furthermore we show that the model yields plasmon-polariton properties in ex-cellent agreement with classical electrodynamics simulations at a much reduced computational cost and at the benefit
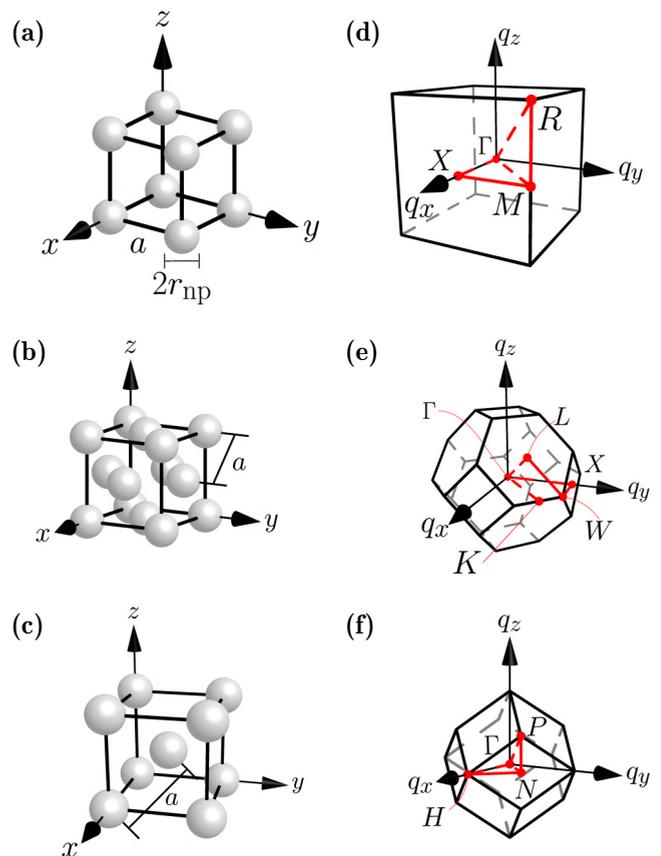
FIG. 1. Conventional unit cells for (a) sc, (b) fcc, and (c) bcc lattices of spherical metallic nanoparticles of radius r_{np} with the primitive lattice parameter a. (d)–(f) Corresponding first Brillouin zones, where the red lines indicate the paths, over which the plasmon and plasmon-polariton dispersions are plotted in Figs. 2–4.

of analytical intuition. With our newly developed tools, we demonstrate that these highly symmetric cubic systems exhibit polarization-dependent optical properties such as band split-tings in the near-infrared or visible range of the spectrum. With the emerging fabrication techniques for 3D metallic nanopar-ticle lattices, this work is an important step towards accurate predictions of their polaritonic properties, and the model can be readily extended to more complex lattices and nanoparticle shapes.

The paper is organized as follows: In Sec. II we describe our theoretical model to study plasmon polaritons. The general so-lution to this model is subsequently presented in Sec. III A. The resulting dispersion relations of the collective plasmons and plasmon polaritons for sc, fcc, and bcc lattices are discussed in Secs. III B and III C, respectively. In Sec. IV, we compare our predictions to classical electrodynamics simulations. We finally summarize our results in Sec. V. In the Appendix we discuss the form of the dielectric tensor that shows a nonlocal response.

II. MODEL

We consider sc, fcc, and bcc lattices of spherical metallic nanoparticles separated by a center-to-center distance a be-tween nearest neighbors, as depicted in Figs. 1(a)–1(c). The

corresponding first Brillouin zones are shown in Figs. 1(d)–1(f). We describe the nanoparticles with a Drude-like dielectric function

$$\epsilon_r^D(\omega) = \epsilon_d - \frac{\omega_p^2}{\omega(\omega + i\gamma^D)}, \qquad (1)$$

where ω_p is the plasma frequency of the considered (noble) metal and where the dielectric constant ϵ_d takes into account the screening of the conduction electrons by the d electrons. In our model we use $\gamma^D = 0$, but we will explore the effect of a nonvanishing Drude damping in the finite-difference frequency-domain (FDFD) calculations, presented in Sec. IV. The surrounding medium that fills the space between the nanoparticles is characterized by the dielectric constant ϵ_m. The magnetic permeabilities of the nanoparticles and the embedding medium are assumed to be equal to the vacuum permeability. Each nanoparticle in the lattice supports three degenerate dipolar LSPs polarized in the x, y, or z direction. They interact with their neighbors through the quasistatic dipole-dipole interaction

$$V_{dip}(\mathbf{R},\mathbf{R}') = \frac{9\epsilon_m}{(\epsilon_d + 2\epsilon_m)^2} \frac{\mathbf{p} \cdot \mathbf{p}' - 3(\mathbf{p} \cdot \hat{n})(\mathbf{p}' \cdot \hat{n})}{4\pi\epsilon_0 |\mathbf{R} - \mathbf{R}'|^3}, \qquad (2)$$

where $\mathbf{p}$ and $\mathbf{p}'$ are the dipole moments associated with the LSPs of the nanoparticles located at the lattice sites $\mathbf{R}$ and $\mathbf{R}'$, respectively, while $\hat{n} = (\mathbf{R} - \mathbf{R}')/|\mathbf{R} - \mathbf{R}'|$, and ϵ_0 is the vacuum permittivity. Here and in what follows, hats denote unit vectors. In the expression above, the prefactor takes into account the two dielectric environments and arises from a model in which each point dipole is located inside a sphere with dielectric constant ϵ_d and separated by a medium with dielectric constant ϵ_m [44]. As we only consider dynamical degrees of freedom relating to the fundamental dipolar LSPs, we are thus neglecting any effects of higher-order multipolar plasmons. This approximation has been shown to be valid for center-to-center interparticle separations $a \gtrsim 3r_{np}$ [13], with r_{np} the nanoparticle radius (see Fig. 1). We demonstrate the validity of this approximation in Sec. IV by comparing our results to FDFD simulations.

We write the full Hamiltonian of the system as

$$H = H_{pl} + H_{ph} + H_{pl\text{-}ph}, \qquad (3)$$

where H_{pl} and H_{ph} denote the plasmonic and photonic Hamiltonians, respectively, and where $H_{pl\text{-}ph}$ is the interaction Hamiltonian between both subsystems. In the Coulomb gauge [42,43], the purely plasmonic Hamiltonian reads [33,34,36,37,39]

$$H_{pl} = \hbar\omega_0 \sum_{\mathbf{q},\hat{\sigma}} b_\mathbf{q}^{\hat{\sigma}\dagger} b_\mathbf{q}^{\hat{\sigma}} + \hbar\Omega \sum_{\mathbf{q},\hat{\sigma},\hat{\sigma}'} f_\mathbf{q}^{\hat{\sigma},\hat{\sigma}'} [b_\mathbf{q}^{\hat{\sigma}\dagger}(b_\mathbf{q}^{\hat{\sigma}'} + b_{-\mathbf{q}}^{\hat{\sigma}'\dagger})$$
$$+ \text{H.c.}], \qquad (4)$$

with

$$f_\mathbf{q}^{\hat{\sigma},\hat{\sigma}'} = \sum_{\substack{\boldsymbol{\rho} \\ (a \leqslant \rho \leqslant \rho_c)}} \left(\frac{a}{\rho}\right)^3 \frac{\cos(\mathbf{q} \cdot \boldsymbol{\rho})}{2}$$
$$\times [\delta_{\hat{\sigma}\hat{\sigma}'} - 3(\hat{\sigma} \cdot \hat{\rho})(\hat{\sigma}' \cdot \hat{\rho})]. \qquad (5)$$

Here, $\mathbf{q} = q\hat{q}$ is the plasmonic wave vector in the first Brillouin zone. In Eq. (4), $b_\mathbf{q}^{\hat{\sigma}} = \mathcal{N}^{-1/2} \sum_\mathbf{R} \exp(-i\mathbf{q} \cdot \mathbf{R}) b_\mathbf{R}^{\hat{\sigma}}$ is defined as the Fourier transform of the bosonic operator $b_\mathbf{R}^{\hat{\sigma}}$, which annihilates an LSP at lattice site $\mathbf{R}$ with polarization $\hat{\sigma} = \hat{x}, \hat{y}$, or $\hat{z}$, where $\mathcal{N}$ is the number of unit cells of the metacrystal. The first term on the right-hand side of Eq. (4) describes the uncoupled LSPs with Mie frequency [41]

$$\omega_0 = \frac{\omega_p}{\sqrt{\epsilon_d + 2\epsilon_m}}, \qquad (6)$$

while the second one with coupling constant

$$\Omega = \frac{3\epsilon_m}{2(\epsilon_d + 2\epsilon_m)} \omega_0 \left(\frac{r_{np}}{a}\right)^3 \qquad (7)$$

corresponds to the Coulomb dipole-dipole interaction [cf. Eq. (2)] between nanoparticles linked by the separation vector $\boldsymbol{\rho}$. Crucially, we consider Coulomb interactions up to a large cutoff distance $\rho_c \gg a$, beyond the nearest-neighbor approximation that was employed in Ref. [39]. As will be highlighted later, these long-range Coulomb interactions are critical for obtaining the correct plasmonic dispersions.

As discussed in detail in Ref. [45], there is a region of slow convergence of $f_\mathbf{q}^{\hat{\sigma},\hat{\sigma}'}$ around the Γ point [see Eq. (5)]. This stems from discontinuities of $f_\mathbf{q}^{\hat{\sigma},\hat{\sigma}'}$ at $\mathbf{q} = 0$ for $\rho_c \to \infty$. These discontinuities lead to the Gibbs-Wilbraham phenomenon [46], and the summation in Eq. (5) does not easily converge with increasing cutoff radius ρ_c. Thus, for small wave vectors $q < \alpha\rho_c^{-1}$, with α a real positive number, we use the correction $f_\mathbf{q}^{\hat{\sigma},\hat{\sigma}'} = -2\pi[\delta_{\hat{\sigma}\hat{\sigma}'} - 3(\hat{\sigma} \cdot \hat{q})(\hat{\sigma}' \cdot \hat{q})]/3\nu$ for the infinite lattice [45]. It contains the factor ν, which accounts for the different volumes of the primitive cells of the considered lattices and equals $\nu = 1$ for sc, $\nu = 2^{-1/2} \simeq 0.71$ for fcc, and $\nu = 4/3^{3/2} \simeq 0.77$ for bcc lattices, respectively.

In Eq. (3) the photonic subsystem is described by

$$H_{ph} = \sum_{\mathbf{q},\hat{\lambda}_\mathbf{q}} \hbar\omega_{ph,\mathbf{q}} c_\mathbf{q}^{\hat{\lambda}_\mathbf{q}\dagger} c_\mathbf{q}^{\hat{\lambda}_\mathbf{q}}, \qquad (8)$$

where $c_\mathbf{q}^{\hat{\lambda}_\mathbf{q}}$ annihilates and $c_\mathbf{q}^{\hat{\lambda}_\mathbf{q}\dagger}$ creates a photon with wave vector $\mathbf{q}$, dispersion $\omega_{ph,\mathbf{q}} = cq/\sqrt{\epsilon_m}$, and transverse polarization $\hat{\lambda}_\mathbf{q}$ (with $\hat{\lambda}_\mathbf{q} \cdot \mathbf{q} = 0$). Here $c/\sqrt{\epsilon_m}$ is the speed of light in the embedding medium. In the long-wavelength limit $qr_{np} \ll 1$, the minimal light-matter coupling Hamiltonian in Eq. (3) takes the form

$$H_{pl\text{-}ph} = i\hbar\omega_0 \sum_{\mathbf{q},\hat{\sigma},\hat{\lambda}_\mathbf{q}} \hat{\sigma} \cdot \hat{\lambda}_\mathbf{q} \xi_\mathbf{q} (b_\mathbf{q}^{\hat{\sigma}\dagger} c_\mathbf{q}^{\hat{\lambda}_\mathbf{q}} + b_\mathbf{q}^{\hat{\sigma}\dagger} c_{-\mathbf{q}}^{\hat{\lambda}_\mathbf{q}\dagger} - \text{H.c.})$$
$$+ \hbar\omega_0 \sum_{\mathbf{q},\hat{\lambda}_\mathbf{q}} \xi_\mathbf{q}^2 (c_\mathbf{q}^{\hat{\lambda}_\mathbf{q}\dagger} c_\mathbf{q}^{\hat{\lambda}_\mathbf{q}} + c_\mathbf{q}^{\hat{\lambda}_\mathbf{q}\dagger} c_{-\mathbf{q}}^{\hat{\lambda}_\mathbf{q}\dagger} + \text{H.c.}), \qquad (9)$$

where $\xi_\mathbf{q} = [2\Omega\pi/(\nu\omega_{ph,\mathbf{q}})]^{1/2}$. Since we consider lattice constants a much smaller than the wavelength associated with the LSP resonances, we neglect Umklapp processes in Eqs. (8) and (9). However, the model can be readily extended to include such Umklapp scattering in order to describe metamaterials with larger lattice constants.

Let us point out that the first term on the right-hand side of Eq. (9) describes, to second-order in perturbation theory, the

exchange of virtual photons among the nanoparticles of the lattice [43]. Such a term therefore incorporates the retardation effects in the dipolar coupling between the LSPs.

III. RESULTS AND DISCUSSION

A. General solution

The full Hamiltonian (3), representing collective plasmons strongly coupled to photons, can be diagonalized by

introducing the bosonic operator

$$
\eta_{\mathbf{q}}^{\hat{\tau}_{\mathbf{q}}} = \sum_{\hat{\sigma}} \left(u_{\mathbf{q}}^{\hat{\tau}_{\mathbf{q}},\hat{\sigma}} b_{\mathbf{q}}^{\hat{\sigma}} + v_{\mathbf{q}}^{\hat{\tau}_{\mathbf{q}},\hat{\sigma}} b_{-\mathbf{q}}^{\hat{\sigma}\dagger} \right) + \sum_{\hat{\lambda}_{\mathbf{q}}} \left(m_{\mathbf{q}}^{\hat{\tau}_{\mathbf{q}},\hat{\lambda}_{\mathbf{q}}} c_{\mathbf{q}}^{\hat{\lambda}_{\mathbf{q}}} + n_{\mathbf{q}}^{\hat{\tau}_{\mathbf{q}},\hat{\lambda}_{\mathbf{q}}} c_{-\mathbf{q}}^{\hat{\lambda}_{\mathbf{q}}\dagger} \right),
$$

$$(10)$$

which annihilates a plasmon polariton with wave vector $\mathbf{q}$ and polarization $\hat{\tau}_{\mathbf{q}}$, the latter being generally not aligned with the $\hat{\sigma}$ axis. Imposing that the operator in Eq. (10) and its adjoint diagonalize the Hamiltonian (3) as

$$
H = \sum_{\mathbf{q},\hat{\tau}_{\mathbf{q}}} \hbar \omega_{\mathrm{pp},\mathbf{q}}^{\hat{\tau}_{\mathbf{q}}} \eta_{\mathbf{q}}^{\hat{\tau}_{\mathbf{q}}\dagger} \eta_{\mathbf{q}}^{\hat{\tau}_{\mathbf{q}}}, \tag{11}
$$

the Heisenberg equation of motion $[\eta_{\mathbf{q}}^{\hat{\tau}_{\mathbf{q}}}, H] = \hbar \omega_{\mathrm{pp},\mathbf{q}}^{\hat{\tau}_{\mathbf{q}}} \eta_{\mathbf{q}}^{\hat{\tau}_{\mathbf{q}}}$ leads to the 10×10 eigensystem

$$
\begin{pmatrix}
\omega_0 \mathbb{1}_3 + 2\Omega F_{\mathbf{q}} & -2\Omega F_{\mathbf{q}} & -i\omega_0 \xi_{\mathbf{q}} P_{\mathbf{q}} & i\omega_0 \xi_{\mathbf{q}} P_{\mathbf{q}} \\
2\Omega F_{\mathbf{q}} & -(\omega_0 \mathbb{1}_3 + 2\Omega F_{\mathbf{q}}) & i\omega_0 \xi_{\mathbf{q}} P_{\mathbf{q}} & -i\omega_0 \xi_{\mathbf{q}} P_{\mathbf{q}} \\
i\omega_0 \xi_{\mathbf{q}} P_{\mathbf{q}}^\top & i\omega_0 \xi_{\mathbf{q}} P_{\mathbf{q}}^\top & (\omega_{\mathrm{ph},\mathbf{q}} + 2\omega_0 \xi_{\mathbf{q}}^2)\mathbb{1}_2 & -2\omega_0 \xi_{\mathbf{q}}^2 \mathbb{1}_2 \\
i\omega_0 \xi_{\mathbf{q}} P_{\mathbf{q}}^\top & i\omega_0 \xi_{\mathbf{q}} P_{\mathbf{q}}^\top & 2\omega_0 \xi_{\mathbf{q}}^2 \mathbb{1}_2 & -(\omega_{\mathrm{ph},\mathbf{q}} + 2\omega_0 \xi_{\mathbf{q}}^2)\mathbb{1}_2
\end{pmatrix}
\begin{pmatrix}
\mathbf{u}_{\mathbf{q}}^{\hat{\tau}_{\mathbf{q}}} \\
\mathbf{v}_{\mathbf{q}}^{\hat{\tau}_{\mathbf{q}}} \\
\mathbf{m}_{\mathbf{q}}^{\hat{\tau}_{\mathbf{q}}} \\
\mathbf{n}_{\mathbf{q}}^{\hat{\tau}_{\mathbf{q}}}
\end{pmatrix}
= \omega_{\mathrm{pp},\mathbf{q}}^{\hat{\tau}_{\mathbf{q}}}
\begin{pmatrix}
\mathbf{u}_{\mathbf{q}}^{\hat{\tau}_{\mathbf{q}}} \\
\mathbf{v}_{\mathbf{q}}^{\hat{\tau}_{\mathbf{q}}} \\
\mathbf{m}_{\mathbf{q}}^{\hat{\tau}_{\mathbf{q}}} \\
\mathbf{n}_{\mathbf{q}}^{\hat{\tau}_{\mathbf{q}}}
\end{pmatrix}, \tag{12}
$$

where the vectors $\mathbf{u}_{\mathbf{q}}^{\hat{\tau}_{\mathbf{q}}}$, $\mathbf{v}_{\mathbf{q}}^{\hat{\tau}_{\mathbf{q}}}$, $\mathbf{m}_{\mathbf{q}}^{\hat{\tau}_{\mathbf{q}}}$, and $\mathbf{n}_{\mathbf{q}}^{\hat{\tau}_{\mathbf{q}}}$ consist of $u_{\mathbf{q}}^{\hat{\tau}_{\mathbf{q}},\hat{\sigma}}$, $v_{\mathbf{q}}^{\hat{\tau}_{\mathbf{q}},\hat{\sigma}}$, $m_{\mathbf{q}}^{\hat{\tau}_{\mathbf{q}},\hat{\lambda}_{\mathbf{q}}}$, and $n_{\mathbf{q}}^{\hat{\tau}_{\mathbf{q}},\hat{\lambda}_{\mathbf{q}}}$, respectively, as defined in Eq. (10). In Eq. (12), $\mathbb{1}_n$ stands for the $n \times n$ identity matrix, the 3×3 symmetric matrix $F_{\mathbf{q}}$ is defined by its elements $f_{\mathbf{q}}^{\hat{\sigma},\hat{\sigma}'}$ as given in Eq. (5), while the 3×2 matrix $P_{\mathbf{q}}$ is introduced as

$$
P_{\mathbf{q}} = \begin{pmatrix}
\hat{x} \cdot \hat{\lambda}_{1,\mathbf{q}} & \hat{x} \cdot \hat{\lambda}_{2,\mathbf{q}} \\
\hat{y} \cdot \hat{\lambda}_{1,\mathbf{q}} & \hat{y} \cdot \hat{\lambda}_{2,\mathbf{q}} \\
\hat{z} \cdot \hat{\lambda}_{1,\mathbf{q}} & \hat{z} \cdot \hat{\lambda}_{2,\mathbf{q}}
\end{pmatrix}, \tag{13}
$$

and $P_{\mathbf{q}}^\top$ represents its transpose. Here, the two photon polarizations can be parameterized, e.g., as $\hat{\lambda}_{1,\mathbf{q}} = \hat{z} \times \hat{q}/|\hat{z} \times \hat{q}|$ and $\hat{\lambda}_{2,\mathbf{q}} = \hat{q} \times \hat{\lambda}_{1,\mathbf{q}}/|\hat{q} \times \hat{\lambda}_{1,\mathbf{q}}|$ for $\hat{q} \nparallel \hat{z}$, while for $\hat{q} = \hat{z}$, we choose $\hat{\lambda}_{1,\mathbf{q}} = \hat{x}$ and $\hat{\lambda}_{2,\mathbf{q}} = \hat{y}$.

We note that the plasmon-polariton eigenfrequencies $\omega_{\mathrm{pp},\mathbf{q}}^{\hat{\tau}_{\mathbf{q}}}$ arising from the eigensystem (12) occur in pairs of positive and negative eigenvalues. Below, we will focus on the physically relevant, positive solutions.

If not stated otherwise, we will use an interparticle distance $a = 3r_{\mathrm{np}}$, a cutoff radius $\rho_{\mathrm{c}} = 150a$, and $\alpha = 10$. We have checked that the latter choices provide numerically-converged results for the collective plasmon and plasmon-polariton dispersions, presented in the next subsections.

B. Collective plasmons

Before considering the fully coupled system, represented by the Hamiltonian (3), it is instructive to analyze in detail the purely plasmonic problem described by H_{pl} in Eq. (4). We will therefore set the light-matter coupling to zero in this

subsection. In this way, plasmon properties are computed in the quasistatic limit, neglecting all retardation effects.

Setting $\xi_{\mathbf{q}} = 0$, the matrix defined in Eq. (12) becomes block diagonal. On one hand, the lower 4×4 block is diagonal and corresponds to the two degenerate photon branches with dispersion $\omega_{\mathrm{ph},\mathbf{q}}$ for the two positive eigenvalues. The three positive eigenvalues of the upper 6×6 block, on the other hand, yield the collective plasmon dispersion $\omega_{\mathrm{pl},\mathbf{q}}^{\hat{\tau}_{\mathbf{q}}}$, which is represented in Fig. 2 as a function of wave vector $\mathbf{q}$ along the red paths given in Figs. 1(d)–1(f) for the sc [Fig. 2(a)], fcc [Fig. 2(b)], and bcc [Fig. 2(c)] lattices. In the figure we use $\epsilon_{\mathrm{d}} = 5.6$, as determined for silver films [47,48], and $\epsilon_{\mathrm{m}} = 4$, mimicking an embedding medium made of glass or polymer. In Fig. 2 we also show the collective plasmon-polarization angle $\phi_{\mathrm{pl},\mathbf{q}}^{\hat{\tau}_{\mathbf{q}}} = \arccos(|\hat{\tau}_{\mathbf{q}} \cdot \hat{q}|)$, where we choose $\hat{\tau}_{\mathbf{q}} = \hat{u}_{\mathbf{q}}^{\hat{\tau}_{\mathbf{q}}}$. Notice that the alternative choice $\hat{\tau}_{\mathbf{q}} = \hat{v}_{\mathbf{q}}^{\hat{\tau}_{\mathbf{q}}}$ leads to the same polarization angle, as the vectors $\mathbf{u}_{\mathbf{q}}^{\hat{\tau}_{\mathbf{q}}}$ and $\mathbf{v}_{\mathbf{q}}^{\hat{\tau}_{\mathbf{q}}}$ are proportional for a given wave vector $\mathbf{q}$. With the above definition of $\phi_{\mathrm{pl},\mathbf{q}}^{\hat{\tau}_{\mathbf{q}}}$, longitudinal collective plasmons, which do not couple to light, have a polarization angle $\phi_{\mathrm{pl},\mathbf{q}}^{\hat{\tau}_{\mathbf{q}}} = 0$ (black lines in Fig. 2), while purely transverse modes have a corresponding polarization $\phi_{\mathrm{pl},\mathbf{q}}^{\hat{\tau}_{\mathbf{q}}} = \pi/2$ (yellow lines in Fig. 2).

Our results in Fig. 2 indicate that there are two purely transverse collective plasmons and one purely longitudinal one along the high-symmetry axes in the first Brillouin zone [i.e., axes with two- to fourfold rotational symmetry, see Figs. 1(d)–1(f)]. For less symmetric axes the collective modes can be of a mixed type [see, e.g., the XM and MR lines in Fig. 2(a)]. Moreover, along three- and fourfold symmetry axes, the two transverse modes are degenerate [see, e.g., the ΓR and ΓX lines in Fig. 2(a)]. This is a manifestation of Neumann's principle [49]: For the collective plasmon dispersion this enforces the
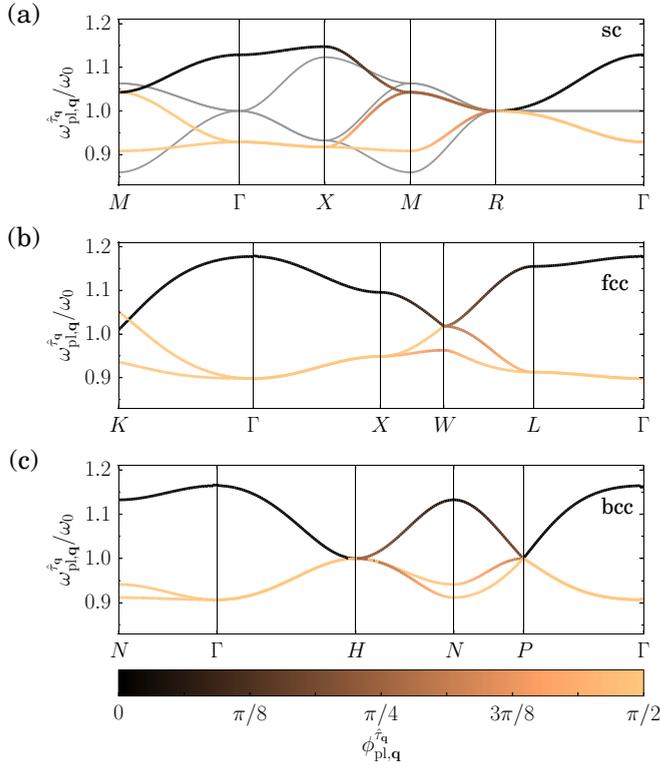
FIG. 2. Collective plasmon dispersion $\omega_{\mathrm{pl},\mathbf{q}}^{\hat{\tau}_{\mathbf{q}}}$ in units of the LSP frequency ω_0 along the paths shown in red in Figs. 1(d)–1(f) for the (a) sc, (b) fcc, and (c) bcc lattices. The color code corresponds to the collective plasmon-polarization angle $\phi_{\mathrm{pl},\mathbf{q}}^{\hat{\tau}_{\mathbf{q}}}$, which equals 0 ($\pi/2$) for purely longitudinal (transverse) plasmons. In the figure we use $a = 3r_{\mathrm{np}}$, $\rho_{\mathrm{c}} = 150a$, and $\alpha = 10$ for the colored thick lines, while in panel (a) we choose $\rho_{\mathrm{c}} = a$ and $\alpha = 0$ for the gray thin lines, corresponding to nearest-neighbor interactions only [cf. Eq. (15)]. In all cases the dielectric constants are set to $\epsilon_{\mathrm{d}} = 5.6$ and $\epsilon_{\mathrm{m}} = 4$.

degeneracy of the transverse modes for the three- and fourfold symmetry lines. The latter degeneracy is lifted for wave-vector directions with lower symmetry. We also note that one would expect the longitudinal and transverse plasmon modes to be degenerate at the Γ point since the latter has the full point-group symmetry of the lattice. As we will see later, there is a radiative correction from the light-matter interaction Hamiltonian (9) that enforces this degeneracy in the polariton spectrum.

Before we move on to the discussion of the fully coupled system, a comment is in order about the importance of the dipole-dipole interaction beyond nearest neighbors for the collective plasmon dispersion. In Fig. 2(a) we represent by thin gray lines the plasmon dispersion of the sc lattice, including nearest-neighbor interactions only. (Note that we do not correct for the Wilbraham-Gibbs phenomenon around the Γ point in this case, i.e., we use $\alpha = 0$.) Under these conditions, the matrix $F_{\mathbf{q}}$ is diagonal, and its elements read

$$f_{\mathbf{q}}^{\hat{\sigma},\hat{\sigma}'} = \delta_{\hat{\sigma}\hat{\sigma}'} \sum_{\hat{\sigma}''=\hat{x},\hat{y},\hat{z}} (1 - 3\delta_{\hat{\sigma}\hat{\sigma}''}) \cos(a\hat{\sigma}'' \cdot \mathbf{q}). \quad (14)$$

The plasmonic Hamiltonian (4) is therefore separable into $\hat{x}$, $\hat{y}$, and $\hat{z}$ directions and can be diagonalized analytically, yielding

$$\omega_{\mathrm{pl},\mathbf{q}}^{\hat{\sigma}} = \omega_0 \sqrt{1 + 4\frac{\Omega}{\omega_0} f_{\mathbf{q}}^{\hat{\sigma},\hat{\sigma}}}. \quad (15)$$

This result and the corresponding coefficients of the Bogoliubov transformation (10), which we do not report explicitly here, coincide with those found in Ref. [39] for LSP polarizations along $\hat{x}$, $\hat{y}$, or $\hat{z}$ and $\epsilon_{\mathrm{m}} = \epsilon_{\mathrm{d}} = 1$. As can be seen in Fig. 2(a), including the dipole-dipole interactions beyond nearest neighbors can have a qualitative effect on the collective plasmon dispersion, most noticeably around the Γ point. They further lift the degeneracy between plasmon branches, e.g., along the ΓM and ΓR directions. In other regions of the first Brillouin zone the difference between the full dispersion and those from nearest neighbors only is less significant.

C. Plasmon polaritons

We now consider the fully coupled system, represented by the eigensystem (12), and numerically solve for its five positive eigenvalues. These eigenvalues yield the plasmon-polariton spectrum $\omega_{\mathrm{pp},\mathbf{q}}^{\hat{\tau}_{\mathbf{q}}}$, which is shown by solid lines in Fig. 3 for the sc [Figs. 3(a)–3(c)], fcc [Figs. 3(d)–3(f)], and bcc lattices [Figs. 3(g)–3(i)] along twofold [Figs. 3(a), 3(d), and 3(g)], threefold [Figs. 3(b), 3(e), and 3(h)], and fourfold symmetry axes [Figs. 3(c), 3(f), and 3(i)], cf. Figs. 1(d)–1(f). Along the high symmetry axes of the first Brillouin zone, the five modes split up into four polaritonic branches (colored solid lines) and one purely longitudinal collective plasmon, which does not couple to transverse photons (black lines). The four polaritonic modes result from the coupling of transverse collective plasmons (see Fig. 2) to photons, whose dispersion relation is shown by dashed lines in Fig. 3. According to the construction of our effective model and the nature of the Coulomb gauge, retardation effects are taken into account for all plasmon-polariton branches, where photons and plasmons interact via Eq. (9).

As can be inferred from Fig. 3, there are two high-energy polaritonic branches (orange solid lines) and two low-energy ones (green solid lines). The two high-energy branches are nearly degenerate. The low-energy polaritonic branches, shown by green solid lines in Fig. 3, have the same twofold degeneracy along threefold and fourfold symmetry axes as the collective plasmon dispersion (compare with Fig. 2) and the light-matter interaction does not lift this degeneracy. As mentioned previously, there is a radiative correction to the transverse plasmonic modes at the Γ point, which is equal to the longitudinal-transverse splitting observed in the plasmonic spectrum (Fig. 2). As a result, one observes that the longitudinal and transverse high-energy polaritonic branches are degenerate at the Γ point (Fig. 3), as required by symmetry.

For wave vectors close to the edge of the first Brillouin zone the high-energy polaritonic branches (orange solid lines in Fig. 3) asymptotically approach the light cone, while the low-energy ones (green solid lines in the figure) tend to the collective plasmon dispersion. For $\mathbf{q} \to 0$ (i.e., close to the Γ point), the states corresponding to the low-energy branches are mostly photonlike, with a renormalized group velocity,
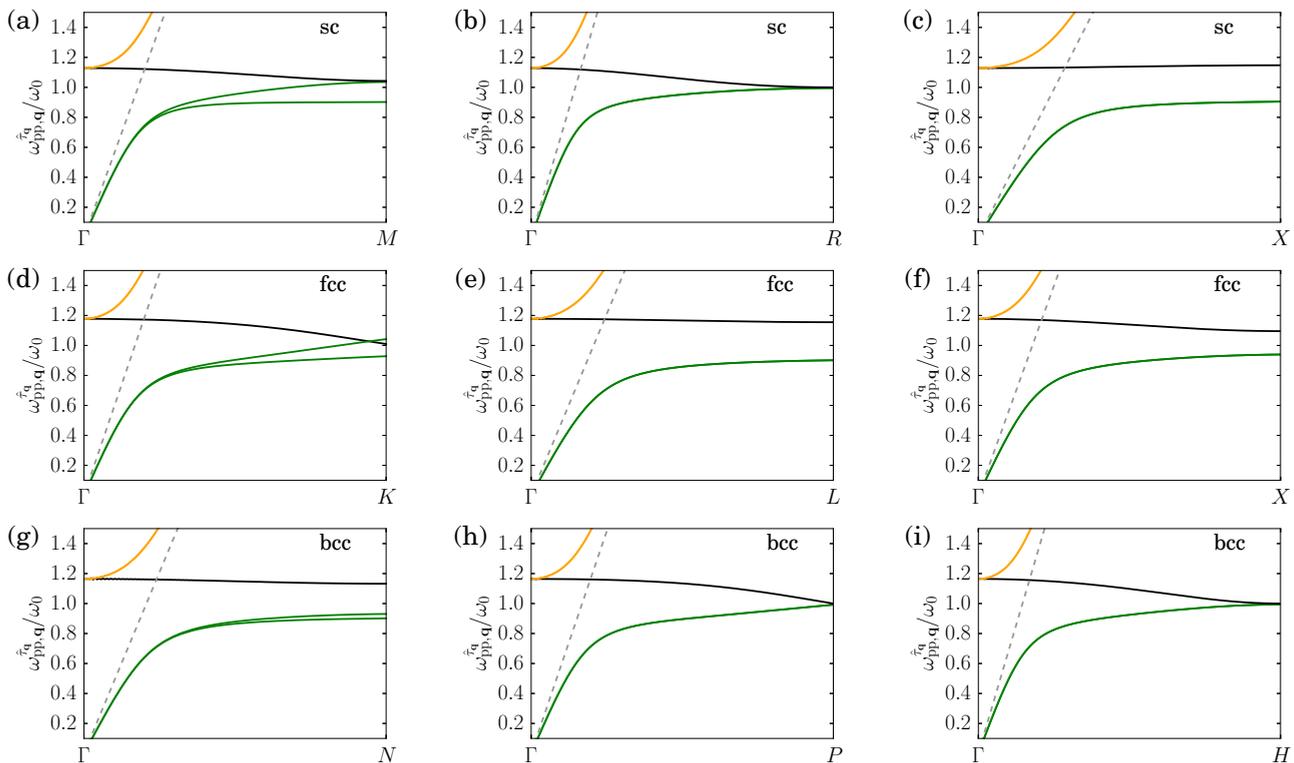
FIG. 3. Solid lines: plasmon-polariton dispersion $\omega_{\mathrm{pp},\mathbf{q}}^{\hat{t}_{\mathbf{q}}}$ in units of the LSP frequency ω_0 for the (a)–(c) sc, (d)–(f) fcc, and (g)–(i) bcc lattices along the (a),(d),(g) twofold, (b),(e),(h) threefold, and (c),(f),(i) fourfold symmetry axes, shown in Fig. 1. Dashed gray lines: free photon dispersion $\omega_{\mathrm{ph},\mathbf{q}}$. The parameters used in the figure are $a = 3r_{\mathrm{np}}$, $\rho_{\mathrm{c}} = 150a$, $\alpha = 10$, $\omega_0 r_{\mathrm{np}}/c = 0.237$, $\epsilon_{\mathrm{d}} = 5.6$, and $\epsilon_{\mathrm{m}} = 4$.

which is smaller than $c/\sqrt{\epsilon_{\mathrm{m}}}$, indicating an effective index of refraction larger than $\sqrt{\epsilon_{\mathrm{m}}}$. However, the high-energy branches do not tend to the values displayed in Fig. 2 at the Γ point due to the strong coupling between collective plasmons and photons [cf. Eq. (9)]. This results in a splitting between the low- and high-energy polaritonic branches. We define this polaritonic splitting $\Delta_{\hat{q}}$ as the frequency difference between the minimum of the high-energy polaritonic branches and the maximum of the lower branches over all wave vectors $\mathbf{q}$ in the first Brillouin zone along a fixed direction $\hat{q}$ from the Γ point.

As can be seen in Fig. 3 for $\epsilon_{\mathrm{d}} = 5.6$ and $\epsilon_{\mathrm{m}} = 4$, the polaritonic splitting reaches values of the order of 25% of the LSP resonance frequency ω_0. For noble-metal nanoparticles the latter typically lies in the visible to ultraviolet range ($\omega_0 \simeq 2$–$4\,\mathrm{eV}/\hbar$), resulting in a splitting of about $\Delta_{\hat{q}} \simeq 0.5$–$1.0\,\mathrm{eV}/\hbar$. The splitting in the polaritonic dispersion has important experimental consequences for the optical properties of the metamaterial. Indeed, along a certain direction $\hat{q}$ in the Brillouin zone, no plasmon polariton can propagate for frequencies within the band gap, so that the reflectivity of the metacrystal should be perfect. We would like to emphasize that the physical origin of these band gaps is entirely different from those emerging in conventional photonic crystals which are the result of Bragg scattering [50]. In fact, we neglect Umklapp processes and therefore the band gaps emerge as a result of polaritonic hybridization between Mie resonances and photons.

Interestingly, the polaritonic splitting depends on the polarization for the twofold symmetry axes of the three cubic lattices [see Figs. 3(a), 3(d), and 3(g)]. This birefringence is directly re-

lated to the polarization dependence of the collective plasmon dispersion, the latter being due to the anisotropic nature of the dipole-dipole interaction between the nanoparticles composing the metamaterial. The modulation of the band splitting can be rather significant for the sc and fcc lattices (around 12% of ω_0), while for the bcc lattice it is comparatively less (around 3% of ω_0). In the following, we will refer to the modulation of $\Delta_{\hat{q}}$ for different polarizations as $\delta_{\hat{q}}$.

Let us now discuss the dependence of the plasmon-polariton dispersions on the dielectric constants ϵ_{d} and ϵ_{m} for the twofold symmetry axes, as shown in Fig. 4. To simplify the discussion, we keep the Mie frequency ω_0 constant in Figs. 4(a) and 4(b) by adjusting ω_{p}, while the Mie frequency is varied in Fig. 4(c). As indicated in Fig. 4(a), an increase in the screening of the core electrons decreases the polaritonic splitting and leads to a corresponding flattening of the longitudinal plasmon branch. The smaller splitting can be understood by noting that the coupling constant $\Omega \propto 1/(2 + \epsilon_{\mathrm{d}}/\epsilon_{\mathrm{m}})$ in the plasmonic part [see Eq. (7)] decreases with increasing ϵ_{d}. The dependence of the polaritonic dispersion on the dielectric constant of the surrounding medium ϵ_{m} is more complex, as displayed in Fig. 4(b). An increasing ϵ_{m} reduces the effective speed of light in the medium. Hence, this reduces the slope of the low-energy polaritonic branches around the Γ point, while the slope of the high-energy polaritonic branches is modified away from the Γ point. Furthermore, with increasing ϵ_{m} a larger polaritonic splitting $\Delta_{\hat{q}}$ as well as increased modulation $\delta_{\hat{q}}$ between the low-energy polaritonic branches of different polarization is observed. We attribute this to two factors. Most importantly the coupling constant Ω increases with
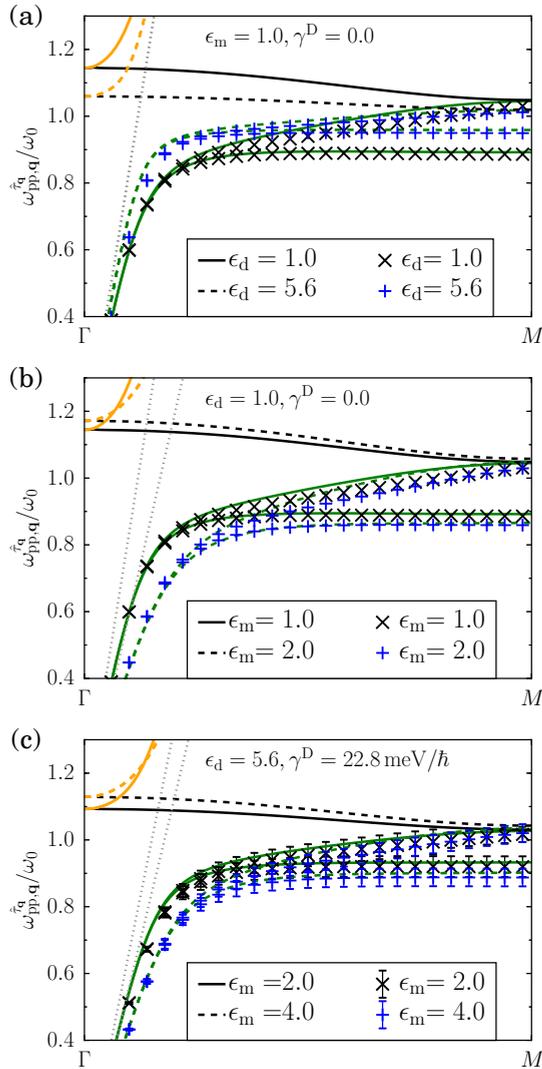
FIG. 4. Plasmon-polariton dispersions for various values of the dielectric constants ϵ_d and ϵ_m. The lines present the results of our Hamiltonian approach [see Eq. (12)] and the symbols those found as solutions in FDFD simulations. Solid and dashed lines: plasmon-polariton dispersions $\omega_{pp,q}^{\hat{\tau}_q}$ in units of the LSP frequency ω_0 for the sc lattice along the twofold symmetry axis (see Fig. 1). Dotted gray lines: free photon dispersions $\omega_{ph,q}$. The parameters for the Hamiltonian approach are $a = 3r_{np}$, $\alpha = 10$, and $\rho_c = 150a$, while we choose $r_{np} = 10$ nm and $a = 3r_{np}$ in the FDFD calculations. In panels (a) and (b) the LSP frequency $\omega_0 r_{np}/c = 0.177$ [see Eq. (6)] is kept constant, while in panel (c) $\omega_p = 9.6$ eV$/\hbar$ is constant. All other parameters are indicated in the respective panels. In the FDFD calculations presented in panel (c), we choose a finite Drude damping γ^D [47], and plot the calculated imaginary parts of the eigenfrequencies, i.e., damping rates, as error bars.

increasing ϵ_m, and thus the related band splittings get larger. An increasing ϵ_m also enhances the plasmon-photon coupling as $\xi_q \propto \epsilon_m^{1/4}/(2 + \epsilon_d/\epsilon_m)^{1/2}$ [see Eq. (9)], but the effect of ξ_q on the polaritonic dispersion is not easily quantified. In Fig. 4(c) the plasma frequency ω_p is fixed to the value of silver films [47,48], while the dielectric constant ϵ_m of the medium is varied. In this case, we observe similar effects as in Fig. 4(b).

We note that for certain high-symmetry axes it is possible to derive analytic expressions for the components of the dielectric tensor of the metamaterial, as we show in the Appendix. Their dependencies on the wave vector and frequency indicate a nonlocal behavior of the metamaterial in space and time.

The experimental observability of the band splittings $\Delta_{\hat{q}}$ and of their polarization-dependent modulation $\delta_{\hat{q}}$, discussed above, may be hindered by damping mechanisms, leading to the decay of the plasmon polaritons. The latter are mostly subject to two sources of damping: Ohmic (absorption) losses with decay rate γ^D inherent to any type of metallic nanostructure [see Eq. (1)], and Landau damping with decay rate γ^L, i.e., the decay of the plasmon excitation into electron-hole pairs [41,51]. Note that radiation damping is irrelevant for the infinite metacrystals considered here since there is no photonic continuum into which the plasmons can decay. Ohmic losses were experimentally estimated to be of the order of $\gamma^D \simeq 24$ meV$/\hbar$ for bulk silver [47]. Moreover, it has been shown that Landau damping only weakly depends on the dipole-dipole interaction [33,34,52], so that we estimate it with the Landau damping of a single nanoparticle. This yields $\gamma^L = 3v_F g/4r_{np}$, where v_F is the Fermi velocity and g is a numerical factor of the order of 1 [41,51,53,54]. For Ag nanoparticles, we obtain $\hbar\gamma^L \simeq 690$ meV$/r_{np}$[nm]. For the nanoparticle radii that we consider (typically of the order of 10 nm), the total linewidth of the plasmon-polariton band structure is therefore of the order of $\gamma^D + \gamma^L \simeq 100$ meV$/\hbar$. For this reason the splittings in the plasmon-polariton dispersion $\Delta_{\hat{q}}$, as well as their polarization dependence $\delta_{\hat{q}}$ for certain directions in the first Brillouin zone, should be experimentally accessible.

IV. COMPARISON TO CLASSICAL ELECTRODYNAMICS SIMULATIONS

To validate the predictions of our Hamiltonian approach presented in the preceding section, we compare them here to calculations based on classical electrodynamics. FDFD simulations are carried out with the electromagnetic wave module of the COMSOL MULTIPHYSICS package with the eigenfrequency solver. We numerically search for solutions to the eigenequation

$$\nabla \times [\nabla \times \mathbf{E}(\mathbf{r},\omega)] - \left(\frac{\omega}{c}\right)^2 \epsilon_r(\mathbf{r},\omega)\mathbf{E}(\mathbf{r},\omega) = 0, \qquad (16)$$

where $\mathbf{E}(\mathbf{r},\omega)$ corresponds to the electric field at position $\mathbf{r}$ and frequency ω, and where $\epsilon_r(\mathbf{r},\omega)$ characterizes the dielectric properties of the metamaterial. We consider an infinite, sc lattice with a lattice constant of 30 nm, which allows us to simplify the numerical calculations by applying Floquet periodicity on the faces of a unit cell for the electric and magnetic fields. We choose nanoparticles of radius 10 nm and model them using the Drude dielectric function of Eq. (1), while in the embedding medium $\epsilon_r(\mathbf{r},\omega) = \epsilon_m$. Note that since we use the eigenvalue solver in COMSOL, we do not insert a driving source into the system. The meshes on three surfaces of the cubic cell are of a free triangular type. They are copied to the opposite side to be compatible with the Floquet periodicity. The cubic cell is filled with an automatically-generated tetrahedral mesh, and the parameters utilized for generating the triangular and tetrahedral meshes are listed in Table I.

TABLE I. Parameters of the triangular and tetrahedral meshes used in the COMSOL simulations.

Maximum element size	2.4 nm
Minimum element size	0.3 nm
Maximum element growth rate	1.45
Curvature factor	0.5
Resolution of narrow regions	0.6
Geometry scaling	1
Adaptive mesh refinement	Not used

The results of the FDFD calculations for the low-energy polaritonic branches are summarized with symbols in Fig. 4. As for the Hamiltonian approach, parameters in Figs. 4(a) and 4(b) are adjusted to give the same Mie frequency $\omega_0 = 3.48$ eV$/\hbar$ for the nanoparticles. In Fig. 4(c) we keep ω_p and ϵ_d constant, varying ϵ_m and exploring the influence of a finite Drude damping γ^D, which is not contained in our Hamiltonian-based model. The parameters ω_p and γ^D are chosen as specified for silver in Ref. [47]. We find an excellent agreement of the FDFD simulations with the predictions of our effective model in all cases, confirming its validity. To avoid repetition, we refrain from discussing in further detail the results of the FDFD calculations in Figs. 4(a) and 4(b), but concentrate on the new aspect due to the inclusion of a finite damping in Fig. 4(c). There, the imaginary part of the eigenfrequencies, which can be interpreted as the linewidth broadening due to Ohmic losses, is represented by error bars. We find a general trend of an increased damping with increasing wave vector. Since the broadenings turn out to have nearly no influence on the polaritonic dispersion relations, our model reproduces the dispersions with great accuracy. The small redshift of the FDFD calculations with respect to our model can be understood by the fact that we neglect Umklapp scattering and higher-order multipolar bands, which would push the bands downward in energy. Even if a wave-vector-independent broadening γ^L due to Landau damping would be added, which we argued to be actually larger than the broadening due to Ohmic losses (see the discussion in Sec. III C), the polarization-dependent band gap modulation $\delta_{\hat{q}}$ should still be observable.

With the distribution of the electric field available in the COMSOL package, we can check the polarization direction that our Hamiltonian approach predicts for the sc lattice. Along the ΓM direction with $\hat{q} = (\hat{x} + \hat{y})/\sqrt{2}$ [see Figs. 1(d) and 4] we find that the lowest-energy transverse plasmon-polariton branch exhibits a polarization $\hat{\tau}_{\mathbf{q}}$ parallel to the $\hat{z}$ axis, while the second lowest-energy one exhibits a polarization $\hat{\tau}_{\mathbf{q}}$ parallel to $\hat{y} - \hat{x}$. This is indeed confirmed by the FDFD calculations for all the parameter sets tested in Fig. 4. An example of the field distributions is given in Figs. 5(a) and 5(b). For different lengths of the reciprocal wave vectors q, these modes change in details like the field distribution in the middle of the nanoparticle or the calculated field strength, but the polarization directions and the overall dumbbell shape remain the same.

We would like to highlight some difficulties in obtaining the polariton dispersions using FDFD calculations. As we are trying to solve a nonlinear equation in 3D, the solver also converges on many unphysical solutions where the electric
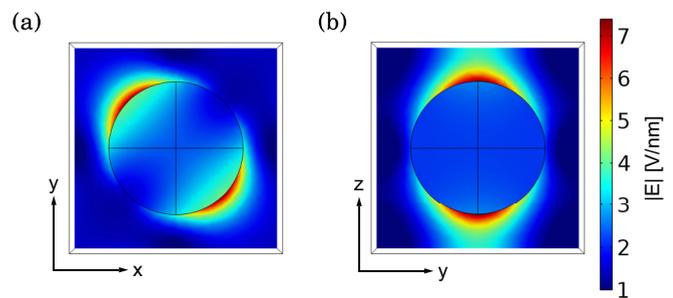
FIG. 5. (a),(b) Density plots for the distribution of the electric field of the low-energy transverse polaritonic modes, shown on a plane cutting through the center of the primitive cell. These distributions are calculated at $\mathbf{q} = 0.49\pi(\hat{x} + \hat{y})/a$ in the direction of the twofold symmetry axis, using the parameters $r_{np} = 10$ nm, $a = 3r_{np}$, $\epsilon_d = 5.6$, $\epsilon_m = 1$, $\omega_p = 9.6$ eV$/\hbar$, and $\gamma^D = 22.8$ meV$/\hbar$ [47]. The dipolar modes exhibit a polarization oriented in the (a) $\hat{y} - \hat{x}$ and (b) $\hat{z}$ directions.

field is, e.g., concentrated in a single spot or exhibits a random-looking distribution. As a result, one has to manually inspect the field profile of the eigenmodes, discarding the artificial solutions and retaining only those with a dipolarlike character, such as the ones shown in Fig. 5. Also, the starting and linearization points for the eigenfrequency search were varied for the different calculations, and we checked that they had negligible effect on the real part of the eigenfrequency. However, we find that the imaginary part is less robust and changes with distance of the real part of the eigenfrequency from the linearization point. For this reason, we took care that the linearization points were located close to the respective eigenfrequencies at each wave vector.

Furthermore, in the discussion above, we have focused on the low-energy polariton branches which show the interesting polarization-dependent band splittings. However, at higher frequencies one can also find, in addition to the longitudinal branch, many polaritonic branches which arise from multipolar plasmon modes.

The excellent agreement of plasmon-polariton dispersions predicted by our Hamiltonian-based model with those of the FDFD simulations shows that higher multipolar modes beyond the considered dipolar interactions as well as intraparticle retardation effects are irrelevant in the studied parameter regime. In addition, we want to point out that the computational costs of our Hamiltonian approach are only a fraction of those of the COMSOL simulations and avoid the cumbersome problems related to the convergence to unphysical solutions. Our Hamiltonian-based approach is thus an efficient way to quantitatively predict the response of metacrystals in the near-field regime, when meta-atom separations are much smaller than the LSP resonance wavelength, i.e., $\omega_0 a/c \ll 1$.

V. CONCLUSIONS

In this paper we have theoretically studied plasmon polaritons in sc, fcc, and bcc lattices of spherical metallic nanoparticles. We have developed a model based on a quantum-mechanical Hamiltonian, justified for small nanoparticles (i.e., with a radius between ca. 1 and 20 nm) in the near-field

dipolar regime. The dipole-dipole interaction between the nanoparticles leads to collective plasmons, which are delocalized over the metacrystal. The strong coupling of these collective plasmons to photons results in the formation of plasmon polaritons.

Our model readily incorporates retardation effects and considers the dielectric properties of the nanoparticles and of the medium in which they are embedded. This has enabled us to derive semianalytical expressions, which determine collective plasmon dispersions, plasmon-polariton dispersions, and their corresponding polarization dependence, and we have analyzed these aspects in detail for the three cubic lattices. We have discussed the influence of the dielectric screening due to core electrons of the nanoparticles and due to the embedding medium on these optical properties. Specifically, we have shown that the polaritonic dispersions present band splittings in the near-infrared to the visible range of the spectrum for all three cubic lattices and for all high-symmetry axes starting from the center of the first Brillouin zone. Remarkably, for special directions in the reciprocal space the polaritonic splitting depends on the polarization, suggesting the possibility to realize a birefringent metacrystal, despite the high degree of cubic symmetry of the latter. By comparing our model to classical electrodynamics simulations, we have shown that it is in quantitative agreement at much reduced computational costs. This robustness emphasizes that the predicted polarization-dependent band dispersions and band splittings should be observable.

APPENDIX: DIELECTRIC TENSOR

In this Appendix, we show that our model of interacting plasmonic nanoparticles leads to a nonlocal, dispersive response. The dielectric tensor of the metamaterial is calculated explicitly for a special, analytically tractable case and is found to depend on both the wave vector and the frequency.

We consider the sc crystal and assume $\mathbf{q} = q\hat{x}$. In this case, the matrix $F_{\mathbf{q}}$ is diagonal and $f_{\mathbf{q}}^{\hat{x},\hat{x}} \neq f_{\mathbf{q}}^{\hat{y},\hat{y}} = f_{\mathbf{q}}^{\hat{z},\hat{z}}$. Furthermore, the choice of $\mathbf{q}$ results in a sparse matrix $P_{\mathbf{q}}$ with the only nonvanishing components being $P_{\mathbf{q}}^{\hat{y},\hat{\lambda}_{1,\mathbf{q}}} = P_{\mathbf{q}}^{\hat{z},\hat{\lambda}_{2,\mathbf{q}}}$. Hence the matrix on the left-hand side of Eq. (12), which we now call $M_{\mathbf{q}}$, can be reordered into a block-diagonal form with block matrices $M_{x,\mathbf{q}} \neq M_{y,\mathbf{q}} = M_{z,\mathbf{q}}$, which read

$$M_{x,\mathbf{q}} = \begin{pmatrix} \omega_0 + 2\Omega f_{\mathbf{q}}^{\hat{x},\hat{x}} & -2\Omega f_{\mathbf{q}}^{\hat{x},\hat{x}} \\ 2\Omega f_{\mathbf{q}}^{\hat{x},\hat{x}} & -\omega_0 - 2\Omega f_{\mathbf{q}}^{\hat{x},\hat{x}} \end{pmatrix} \tag{A1}$$

and

$$M_{y,\mathbf{q}} = \begin{pmatrix} \omega_0 + 2\Omega f_{\mathbf{q}}^{\hat{y},\hat{y}} & -2\Omega f_{\mathbf{q}}^{\hat{y},\hat{y}} & -i\omega_0\xi_{\mathbf{q}} & i\omega_0\xi_{\mathbf{q}} \\ 2\Omega f_{\mathbf{q}}^{\hat{y},\hat{y}} & -\omega_0 - 2\Omega f_{\mathbf{q}}^{\hat{y},\hat{y}} & i\omega_0\xi_{\mathbf{q}} & -i\omega_0\xi_{\mathbf{q}} \\ i\omega_0\xi_{\mathbf{q}} & i\omega_0\xi_{\mathbf{q}} & \omega_{\mathrm{ph},\mathbf{q}} + 2\omega_0\xi_{\mathbf{q}}^2 & -2\omega_0\xi_{\mathbf{q}}^2 \\ i\omega_0\xi_{\mathbf{q}} & i\omega_0\xi_{\mathbf{q}} & 2\omega_0\xi_{\mathbf{q}}^2 & -\omega_{\mathrm{ph},\mathbf{q}} - 2\omega_0\xi_{\mathbf{q}}^2. \end{pmatrix}. \tag{A2}$$

The matrix $M_{x,\mathbf{q}}$ leads to the longitudinal plasmon, which does not couple to light within our model. For this reason, we concentrate on the transverse components. We follow Hopfield [40] to find an expression for the transverse components of the dielectric tensor of the metamaterial $\epsilon_{\mathrm{meta}}^{\hat{y},\hat{y}}(\mathbf{q},\omega) = \epsilon_{\mathrm{meta}}^{\hat{z},\hat{z}}(\mathbf{q},\omega)$. For this purpose, we calculate $\det(M_{y,\mathbf{q}} - \omega^2 \mathbb{1}_4) = 0$ and substitute the definition of the dielectric function $c^2 q^2 = \epsilon_{\mathrm{meta}}^{\hat{y},\hat{y}}(\mathbf{q},\omega)\omega^2$ in the resulting expressions. Solving for $\epsilon_{\mathrm{meta}}^{\hat{y},\hat{y}}(\mathbf{q},\omega)$ and exploiting the plasmonic dispersion relation

$(\omega_{\mathrm{pl},\mathbf{q}}^{\hat{y}})^2 = \omega_0^2 + 4\Omega\omega_0 f_{\mathbf{q}}^{\hat{y},\hat{y}}$ finally yields

$$\epsilon_{\mathrm{meta}}^{\hat{y}\hat{y}}(\mathbf{q},\omega) = \epsilon_{\mathrm{m}} \left[1 + \frac{8\pi\Omega\omega_0}{\left(\omega_{\mathrm{pl},\mathbf{q}}^{\hat{y}}\right)^2 - \omega^2} \right]. \tag{A3}$$

Equation (A3) is the same expression as Eq. (21) in Ref. [39] for $\epsilon_{\mathrm{m}} = \epsilon_{\mathrm{d}} = 1$ and for the respective polarization of the collective plasmon, but we consider here the dipole-dipole interaction beyond the nearest-neighbor limit.

[1] W. L. Barnes, A. Dereux, and T. W. Ebbesen, Surface plasmon subwavelength optics, Nature (London) **424**, 824 (2003).

[2] S. A. Maier, *Plasmonics: Fundamentals and Applications* (Springer, New York, 2007).

[3] N. J. Halas, S. Lal, W.-S. Chang, S. Link, and P. Nordlander, Plasmons in strongly coupled metallic nanostructures, Chem. Rev. **111**, 3913 (2011).

[4] N. Meinzer, W. L. Barnes, and I. R. Hooper, Plasmonic meta-atoms and metasurfaces, Nat. Photon. **8**, 889 (2014).

[5] V. M. Shalaev, Transforming light, Science **322**, 384 (2008).

[6] M. S. Tame, K. R. McEnery, S. K. Ozdemir, J. Lee, S. A. Maier, and M. S. Kim, Quantum plasmonics, Nat. Phys. **9**, 329 (2013).

[7] M. B. Ross, C. A. Mirkin, and G. C. Schatz, Optical properties of one-, two-, and three-dimensional arrays of plasmonic nanostructures, J. Phys. Chem. C **120**, 816 (2015).

[8] S. J. Tan, M. J. Campolongo, D. Luo, and W. Cheng, Building plasmonic nanostructures with DNA, Nat. Nanotechnol. **6**, 268 (2011).

[9] Y. Kim, R. J. Macfarlane, M. R. Jones, and C. A. Mirkin, Transmutable nanoparticles with reconfigurable surface ligands, Science **351**, 579 (2016).

[10] W. Liu, M. Tagawa, H. L. Xin, T. Wang, H. Emamy, H. Li, K. G. Yager, F. W. Starr, A. V. Tkachenko, and O. Gang, Diamond family of nanoparticle superlattices, Science **351**, 582 (2016).

[11] L. Malassis, D. Jishkariani, C. B. Murray, and B. Donnio, Dendronization-induced phase-transfer, stabilization and self-assembly of large colloidal Au nanoparticles, Nanoscale **8**, 13192 (2016).

[12] M. Quinten, A. Leitner, J. R. Krenn, and F. R. Aussenegg, Electromagnetic energy transport via linear chains of silver nanoparticles, Opt. Lett. **23**, 1331 (1998).

[13] M. L. Brongersma, J. W. Hartman, and H. A. Atwater, Electro-magnetic energy transfer and switching in nanoparticle chain arrays below the diffraction limit, Phys. Rev. B **62**, R16356 (2000).

[14] S. A. Maier, P. G. Kik, and H. A. Atwater, Optical pulse propagation in metal nanoparticle chain waveguides, Phys. Rev. B **67**, 205402 (2003).

[15] S. Y. Park and D. Stroud, Surface-plasmon dispersion relations in chains of metallic nanoparticles: An exact quasistatic calculation, Phys. Rev. B **69**, 125418 (2004).

[16] W. H. Weber and G. W. Ford, Propagation of optical excitations by dipolar interactions in metal nanoparticle chains, Phys. Rev. B **70**, 125429 (2004).

[17] D. S. Citrin, Coherent excitation transport in metal-nanoparticle chains, Nano Lett. **4**, 1561 (2004).

[18] C. R. Simovski, A. J. Viitanen, and S. A. Tretyakov, Resonator mode in chains of silver spheres and its possible application, Phys. Rev. E **72**, 066606 (2005).

[19] D. S. Citrin, Plasmon-polariton transport in metal-nanoparticle chains embedded in a gain medium, Opt. Lett. **31**, 98 (2006).

[20] A. F. Koenderink and A. Polman, Complex response and polariton-like dispersion splitting in periodic metal nanoparticle chains, Phys. Rev. B **74**, 033402 (2006).

[21] V. A. Markel and A. K. Sarychev, Propagation of surface plasmons in ordered and disordered chains of metal nanospheres, Phys. Rev. B **75**, 085426 (2007).

[22] K. H. Fung and C. T. Chan, Plasmonic modes in periodic metal nanoparticle chains: A direct dynamic eigenmode analysis, Opt. Lett. **32**, 973 (2007).

[23] A. F. Koenderink, Plasmon nanoparticle array waveguides for single photon and single plasmon sources, Nano Lett. **9**, 4228 (2009).

[24] T. Samrowski, L. Raguin, C. Hafner, and R. Vahldieck, Modelling light propagation in plasmonic nanostructures, Proc. SPIE **7717**, 771707 (2010).

[25] M. Petrov, Disorder-induced Purcell enhancement in nanoparticle chains, Phys. Rev. A **91**, 023821 (2015).

[26] E. Moreno, D. Erni, and C. Hafner, Band structure computations of metallic photonic crystals with the multiple multipole method, Phys. Rev. B **65**, 155120 (2002).

[27] C. Hafner, C. Xudong, and R. Vahldieck, Metallic photonic crystals at optical frequencies, J. Comput. Theor. Nanosci. **2**, 240 (2005).

[28] A. García-Martín, G. Armelles, and S. Pereira, Light transport in photonic crystals composed of magneto-optically active materials, Phys. Rev. B **71**, 205116 (2005).

[29] T. Sannomiya, O. Scholder, K. Jefimovs, C. Hafner, and A. B. Dahlin, Investigation of plasmon resonances in metal films with nanohole arrays for biosensing applications, Small **7**, 1653 (2011).

[30] P. Markoš and V. Kuzmiak, Coupling between Fano and Bragg bands in the photonic band structure of two-dimensional metallic photonic structures, Phys. Rev. A **94**, 033845 (2016).

[31] E. Y. Santiago and R. Esquivel-Sirvent, Optical properties of anisotropic 3D nanoparticles arrays, Europhys. Lett. **119**, 27005 (2017).

[32] C. Lee, M. Tame, J. Lim, and J. Lee, Quantum plasmonics with a metal nanoparticle array, Phys. Rev. A **85**, 063823 (2012).

[33] A. Brandstetter-Kunc, G. Weick, C. A. Downing, D. Weinmann, and R. A. Jalabert, Nonradiative limitations to plasmon propagation in chains of metallic nanoparticles, Phys. Rev. B **94**, 205432 (2016).

[34] C. A. Downing and G. Weick, Topological collective plasmons in bipartite chains of metallic nanoparticles, Phys. Rev. B **95**, 125426 (2017).

[35] C. A. Downing, E. Mariani, and G. Weick, Retardation effects on the dispersion and propagation of plasmons in metallic nanoparticle chains, J. Phys.: Condens. Matter **30**, 025301 (2018).

[36] G. Weick, C. Woollacott, W. L. Barnes, O. Hess, and E. Mariani, Dirac-like Plasmons in Honeycomb Lattices of Metallic Nanoparticles, Phys. Rev. Lett. **110**, 106801 (2013).

[37] T. J. Sturges, C. Woollacott, G. Weick, and E. Mariani, Dirac plasmons in bipartite lattices of metallic nanoparticles, 2D Mater. **2**, 014008 (2015).

[38] C.-R. Mann, T. J. Sturges, G. Weick, W. L. Barnes, and E. Mariani, Manipulating type-I and type-II Dirac polaritons in cavity-embedded honeycomb metasurfaces, arXiv:1707.04503.

[39] G. Weick and E. Mariani, Tunable plasmon polaritons in arrays of interacting metallic nanoparticles, Eur. Phys. J. B **88**, 7 (2015).

[40] J. J. Hopfield, Theory of the contribution of excitons to the complex dielectric constant of crystals, Phys. Rev. **112**, 1555 (1958).

[41] U. Kreibig and M. Vollmer, *Optical Properties of Metal Clusters* (Springer, Berlin, 1995).

[42] C. Cohen-Tannoudji, J. Dupont-Roc, and G. Grynberg, *Atom-Photon Interactions: Basic Processes and Applications* (John Wiley & Sons, New York, 1992).

[43] D. P. Craig and T. Thirunamachandran, *Molecular Quantum Electrodynamics* (Academic Press, London, 1984).

[44] E. Riande and R. Díaz-Calleja, *Electrical Properties of Polymers* (Marcel Dekker, New York, 2004).

[45] M. H. Cohen and F. Keffer, Dipolar sums in the primitive cubic lattices, Phys. Rev. **99**, 1128 (1955).

[46] E. Hewitt and R. E. Hewitt, The Gibbs-Wilbraham phenomenon: An episode in Fourier analysis, Arch. Hist. Exact Sci. **21**, 129 (1979).

[47] M. G. Blaber, M. D. Arnold, and M. J. Ford, Search for the ideal plasmonic nanoshell: The effects of surface scattering and alternatives to gold and silver, J. Phys. Chem. C **113**, 3041 (2009).

[48] H. U. Yang, J. D'Archangel, M. L. Sundheimer, E. Tucker, G. D. Boreman, and M. B. Raschke, Optical dielectric function of silver, Phys. Rev. B **91**, 235137 (2015).

[49] J. F. Nye, *Physical Properties of Crystals* (Oxford University Press, Oxford, 1985).

[50] M. V. Rybin, D. S. Filonov, K. B. Samusev, P. A. Belov, Y. S. Kivshar, and M. F. Limonov, Phase diagram for the transition from photonic crystals to dielectric metamaterials, Nat. Commun. **6**, 10102 (2015).

[51] A. Kawabata and R. Kubo, Electronic properties of fine metallic particles - II. Plasma resonance absorption, J. Phys. Soc. Jpn. **21**, 1765 (1966).

[52] A. Brandstetter-Kunc, G. Weick, D. Weinmann, and R. A. Jalabert, Decay of dark and bright plasmonic modes in a metallic nanoparticle dimer, Phys. Rev. B **91**, 035431 (2015); **92**, 199906(E) (2015).

[53] C. Yannouleas and R. A. Broglia, Landau damping and wall dissipation in large metal clusters, Ann. Phys. (NY) **217**, 105 (1992).

[54] G. Weick, R. A. Molina, D. Weinmann, and R. A. Jalabert, Lifetime of the first and second collective excitations in metallic nanoparticles, Phys. Rev. B **72**, 115410 (2005).